

# Automated Image Processing for the Analysis of DNA Repair Dynamics

Thorsten Rieß<sup>1</sup>   Christian Dietz<sup>1,2</sup>   Martin Tomas<sup>3</sup>   Elisa Ferrando-May<sup>1,3</sup>   Dorit Merhof<sup>1,4</sup>

<sup>1</sup> Interdisciplinary Center for Interactive Data Analysis, Modelling and Visual Exploration (INCIDE)

<sup>2</sup> Department of Physics, Center for Applied Photonics (CAP)

<sup>3</sup> Department of Biology, Bioimaging Center (BIC)

<sup>4</sup> Department of Computer Science, Visual Computing

Universität Konstanz, 78457 Konstanz, Germany

E-Mail: {thorsten.riess,christian.dietz,martin.tomas,elisa.may,dorit.merhof}@uni-konstanz.de

*Abstract*—The efficient repair of cellular DNA is essential for the maintenance and inheritance of genomic information. In order to cope with the high frequency of spontaneous and induced DNA damage, a multitude of repair mechanisms have evolved. These are enabled by a wide range of protein factors specifically recognizing different types of lesions and finally restoring the normal DNA sequence. This work focuses on the repair factor XPC (xeroderma pigmentosum complementation group C), which identifies bulky DNA lesions and initiates their removal via the nucleotide excision repair pathway. The binding of XPC to damaged DNA can be visualized in living cells by following the accumulation of a fluorescent XPC fusion at lesions induced by laser microirradiation in a fluorescence microscope.

In this work, an automated image processing pipeline is presented which allows to identify and quantify the accumulation reaction without any user interaction. The image processing pipeline comprises a preprocessing stage where the image stack data is filtered and the nucleus of interest is segmented. Afterwards, the images are registered to each other in order to account for movements of the cell, and then a bounding box enclosing the XPC-specific signal is automatically determined. Finally, the time-dependent relocation of XPC is evaluated by analyzing the intensity change within this box.

Comparison of the automated processing results with the manual evaluation yields qualitatively similar results. However, the automated analysis provides more accurate, reproducible data with smaller standard errors.

The image processing pipeline presented in this work allows for an efficient analysis of large amounts of experimental data with no user interaction required.

*Keywords*—automated intensity measurement, DNA repair, fluorescence microscopy.

## I. INTRODUCTION

Damage to the DNA of cells occurs either due to environmental factors (*exogenous damage*) or due to natural metabolic processes (*endogenous damage*). Exogenous damage may be caused by exposure to UV light or other types of radiation including  $\gamma$ -rays, or toxins and chemicals. Endogenous damage is mostly caused by reactive oxygen species produced from normal metabolic byproducts, and also includes replication errors during mitosis.

DNA damage occurs at a rate of 1,000 to 1,000,000 molecular lesions per cell per day [1], affecting only 0.000165% of the human genome's approximately 6 billion bases (3 billion base pairs). However, unrepaired damage in critical genes (such as tumor suppressor genes) can interfere with normal

cell physiology and increase the likelihood of tumor formation significantly.

Nucleotide excision repair (NER) [2] is a fundamental protective system that promotes genome stability by eliminating a wide range of DNA lesions. Transcription-coupled repair (TCR), which takes place when the transcription machinery is blocked by obstructing lesions in the transcribed strand [3], and global genome repair (GGR) are the two alternative mechanisms of the NER pathway.

The xeroderma pigmentosum group C (XPC) protein is an important protein involved in the GGR pathway. It recognizes DNA damage and initiates the DNA excision repair of helix-distorting base lesions. In healthy cells, the damage is excised by endonucleases, the missing sequence is replaced by DNA polymerase, and a ligase completes the reaction.

An important research question in the field of DNA repair concerns the mechanisms by which the sensor-like protein XPC actually finds base lesions among a large excess of native DNA in a typical mammalian genome [4], [5]. One approach to investigate how XPC searches for aberrant sites within the DNA consists in the visualization of the time-dependent relocation of fluorescently labeled XPC to sites of DNA damage induced at high spatial resolution by irradiation with a femtosecond laser [6]. For this purpose, XPC was marked with green fluorescent protein (GFP), which allows to investigate the damage-dependent recruitment of the fusion product XPC-GFP by confocal microscopy.

In the analysis pursued in [6] the accumulation of XPC-GFP at the induced lesions was quantified by manually defining a bounding box enclosing the lesion and measurement of the intensity change due to accumulation of XPC-GFP in this box over time.

From an image processing point of view, such a manual analysis is unsatisfactory and error-prone for several reasons: First of all, a manual analysis of a significant amount of mammalian cells is a tedious and time consuming task for the investigator. Furthermore, the results obtained from a manual analysis are not rater-independent and lack robustness and reproducibility.

The challenges for implementing an automated image processing pipeline are due to the low resolution of the image

stacks, due to movements of the cells over time, due to other obscuring cells and structures, and due to the low contrast between the DNA damage and the surrounding nucleus. An overview of current methods for the analysis of fluorescent microscopy images can be found in [7] and references therein.

In this work, these issues are addressed and an automated image processing approach is proposed. This approach allows for automatically detecting the region of XPC accumulation on image stacks showing the cell nuclei and for evaluating the damage-induced changes of XPC dynamics in the nuclear compartment over time. The approach comprises a preprocessing stage, where the image stack data is filtered and the nucleus under consideration is segmented in each image. The images are then registered to each other in order to account for movements of the cell and a bounding box enclosing the DNA damage is automatically determined. Finally, the time-dependent relocation of XPC is evaluated by analyzing the intensity change due to accumulation of XPC-GFP.

## II. MATERIAL AND METHODS

In this section, the image acquisition and the image processing methods for evaluating the time-dependent relocation of XPC-GFP are presented. The microscopy image stacks are acquired in an experimental setup explained in Section II-A. The image stacks are then imported into the software framework KNIME, which is described in section II-B, where the image processing pipeline is implemented. This pipeline consists of a segmentation and registration step as shown in section II-C and the detection of the region of interest (ROI). A scoring algorithm for this detection is presented in section II-D. Finally, the pixel intensity measurement within the ROI is explained in section II-E.

### A. Biological model system and image data acquisition

Recruitment of the DNA repair factor XPC to sites of DNA damage was monitored in live cells by confocal microscopy. To this end fluorescent fusions of wildtype (WT) XPC and of various XPC mutants (F733A, F756A, F797A, F799A, N754A, W531A, W542A, W690A, W690S) were expressed in either Simian virus 40-transformed human XP-C fibroblasts or in Chinese Hamster Ovary cells (CHO). Cells were then irradiated at the microscope stage (Zeiss LSM 5 Pascal) using an in-house built femtosecond Er: fiber laser focused through a 40x oil immersion objective lens. DNA lesions were induced at  $775\text{nm}$  by multiphoton absorption [8]. A cell nucleus expressing XPC-GFP was placed in the center of the field of view and imaged prior to and at defined time intervals after femtosecond laser irradiation. XPC-GFP fluorescence was detected using a  $488\text{nm}$  Ar-laser. The acquired image stacks consist of one pre-irradiation frame, one dark frame recorded while scanning with the fiber laser and 60 or 52 post-irradiation frames for experiments with XP-C cells and CHO cells, respectively. The frames were acquired at time steps of 6–7 seconds and the frame size is either  $512 \times 512$  pixels or  $580 \times 580$  pixels. The femtosecond laser was scanned along a vertical line of  $10\mu\text{m}$  in length [6], [9].

### B. Software framework

The software platform KNIME (The Konstanz Information Miner [10]) is an open-source tool for data integration, processing, analysis and exploration. Essentially, KNIME is designed to import, transform and visualize large data sets in a convenient and easy to use way. KNIME workflows consist of interacting nodes, which may each represent an algorithm, a single import routine or a visualization tool. The exchange of data between nodes is accomplished via data tables which are passed from one node to another by node connections. The graphical user interface makes it possible to construct workflows consisting of different nodes and their interconnection via a simple drag-and-drop mechanism. The data flow is visually represented by connections between the nodes, typically starting with a node to import the data, followed by one or more processing nodes and finally one or more output nodes. Recently, KNIME has been extended to provide basic image processing nodes such as image input/output and standard thresholding algorithms.

In this work, KNIME is used as a basis to implement a fully automated system that measures fluorescence and quantifies the accumulation of XPC-GFP. The image processing workflow consists of several custom KNIME nodes that are combined with standard image processing nodes. This concept allows to batch process large amounts of image stacks and automatically save the results. Additionally, due to the modular design of KNIME workflows, it is possible to assess intermediate results at every stage of the processing pipeline.

### C. Segmentation and registration

The image processing steps required to quantify the accumulation kinetics of XPC comprise the segmentation of the nucleus, a registration step, and the identification of the irradiated area (the ROI).

In order to identify the nucleus of interest (NOI) in each frame of the image stack, the image is smoothed using a standard Median filter with radius three, and an Otsu thresholding algorithm [11] is applied. This results in a coarse segmentation of each NOI candidate. Since the region scanned during image acquisition is adjusted such that the NOI is located at the center of the image, the NOI can be identified even if multiple cell nuclei are visible in the image by comparing the center of gravity of the NOI candidates. The center of gravity of the NOI is then used to create a polar image [12], [13], which is convolved with a Gaussian Blur filter with  $\sigma = 2$  and a standard Median filter of radius three. Then Otsu thresholding is applied to the filtered polar image, which results in a binary image separating the nucleus from the background. In this binary image, the contour of the nucleus can easily be detected. Finally, the original image is masked using this contour, which concludes the segmentation process. The usage of the polar image improves the segmentation result over pure smoothing and thresholding the cartesian image. To get the same result on the cartesian image only, one would need a much more elaborate pipeline than in the proposed approach.

Figure 1 illustrates the different steps of the segmentation process and shows the original image including the NOI and

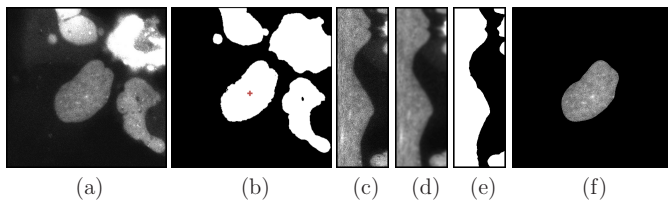


Fig. 1. Segmentation process for an exemplary image. (a) Original image with the nucleus of interest (NOI) in the middle and surrounding (undamaged) objects. (b) Binary image after a Otsu thresholding, the center of gravity of the NOI is marked. (c) Polar image. (d) Smoothed polar image. (e) Binary image resulting from thresholding the smoothed polar image. (f) Masked original image (segmentation result).

surrounding nuclei (a), then the Otsu-thresholded image with the marked center of gravity (b) and the polar image (c). Panel (d) shows the smoothed polar image, which is again thresholded and the binary image is shown in panel (e). The final result is the masked original image shown in panel (f). The resulting segmentation is very accurate and suitable for further processing steps.

In the next step, registration of the individual frames is required due to potential movement and deformation of the nucleus over time. For this purpose, a rigid body registration algorithm [14] is applied to the cropped images from the previous segmentation step. As a result, the position of the NOI remains the same across all frames, and also the area of induced damage remains stationary. This allows us to determine a single ROI which comprises the area of intensity change due to accumulation of XPC-GFP for all image frames in the stack. In very rare cases the nucleus deforms during image acquisition and this deformation also affects the treated area. The rigid body registration does not compensate for this deformation, hence the ROI that is used in the following step is chosen slightly larger than necessary if the nucleus does not deform, but still gives a sufficient accuracy.

#### D. Detection of the area of XPC-GFP accumulation

In order to detect the ROI, a time-averaging projection, avg- $t$ -projection for short, of the registered image stack is created in a first step. In this projection, the damaged area is expected to show up as a vertical line of high intensity. In some example image stacks, this area can be clearly identified also by a non-expert, in others it is at the limit of visual detection. The ROI is a box of fixed size that exactly covers the irradiated area; for the automatic detection the user can adjust the exact width and height that is used in the algorithm. The box orientation is always such that the long side is vertical, since the irradiated area is a vertical line segment, and the movement/deformation of the nucleus after registration is negligible.

For the automated detection of the correct region, a sum- $y$ -projection is applied to the avg- $t$ -projection image, which sums up the intensity values for each column of the image. This results in an intensity profile of the columns, where the damaged area is expected to show up as a peak. A Median filter with radius three is applied to this intensity profile for smoothing. Due to noise, poor image quality and additional bright spots in the nucleus, this peak is not unique and not

straight-forward to identify in some experimental images. For this reason, a combination of three different scoring methods is employed to detect the correct peak. The first scoring method is the height of the peak compared to the neighbouring peaks. The second score is obtained by calculating the response of a “Haar-like” feature [15] centered at the peak and with a fixed width slightly larger than the width of the ROI. This can be interpreted as locally measuring the difference of the area underneath the peak with neighbouring areas. Finally, the third score is the distance of the peak to the center of the nucleus. In an ideal experiment, the irradiation is applied exactly at the center of the NOI, and hence a peak close to the center is more likely to be the correct one. For the automatic evaluation all three scores are weighted equally and the peak with the highest overall score is chosen.

After the correct peak has been identified, the ROI is chosen such that it is centered at the  $x$ -position of the peak and has the predefined width and height. If the height of the nucleus exceeds the height of the ROI, the  $y$ -position of the ROI is adjusted such that the intensity in the avg- $t$ -projection is maximized. Examples are shown in Figure 3 below.

#### E. Intensity measurement

The time-dependent relocation of XPC is evaluated by analyzing the intensity change due to accumulation of XPC-GFP. The measurement is performed on the pre-processed and registered image stack and is accomplished as follows: First, the background is subtracted from the ROI for each image frame in order to improve the results of the intensity measurement. The average pixel intensity of the region of interest  $I_{ROI}$ , as well as the average pixel intensity value  $I_{NOI}$  of the whole NOI, is then measured at every time-step. The quotient  $I_{ROI}/I_{NOI}$  of these values is computed and scaled such that the value of the first image (pre-irradiation) is always equal to one.

In order to validate the presented approach, time-lapse series of a total of 11 different XPC mutants have been analyzed, with each series repeated at least 8 times. The XPC mutants were expressed in two different cell types, human XPC fibroblasts and CHO cells.

The measurement values for each mutant and each cell type were averaged at each time-step and the standard errors were computed, which allows easy comparison to the manual evaluation described in [6], [9].

### III. RESULTS

The results of the automated measurement are presented in the following. In particular, the segmentation performance is evaluated in section III-A, and the measurement results are compared to the manual evaluation in section III-B.

#### A. Segmentation Performance

In order to evaluate the image processing pipeline proposed in this work, approximately 100 image stacks with 52 or 60 frames per stack were processed. The processing pipeline comprises a user interface which is presented to the user

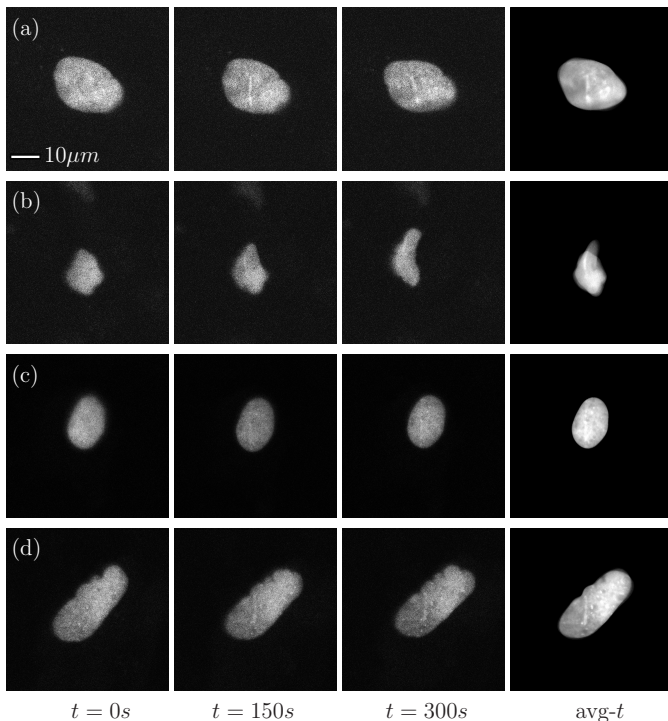


Fig. 2. Microscopy images. Each row shows four images, the first one recorded at the beginning of the experiment (pre-irradiation), the second after 150 seconds and the third after 300 seconds. The fourth image shows the *avg-t* projection *after* the segmentation and registration algorithm has been applied. The XPC-GFP accumulation within the nucleus in row (a) is clearly visible. The nucleus in row (b) deforms and moves during image acquisition. Row (c) shows a nucleus where the accumulation is hardly detectable. The whole nucleus in row (d) is very bright, hence the XPC-GFP accumulation is hardly visible. Note that all microscopy images shown here are contrast enhanced.

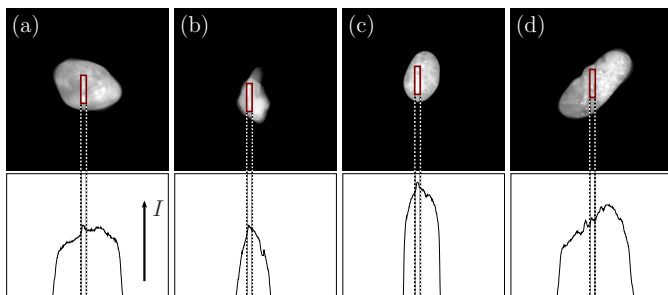


Fig. 3. The detection of the ROI. The top row shows representative images of *avg-t*-projections, the bottom row shows the associated intensity profile, the intensity is denoted by  $I$ . The detected ROI is marked in each *avg-t*-projection image, as well as the associated peak in the intensity profile. The panels (a)–(d) correspond to the images shown in Figure 2 (a)–(d). Note that panel (d) shows a negative example: the irradiated area lies to the left of the incorrectly determined ROI.

at the end of the analysis and allows to review the results. The segmentation results were verified by an expert biologist who rejected image stacks where the first or second image processing step failed.

The first processing step (segmentation of the nuclei) was successful in almost 99% of all cases. Out of the correctly segmented image stacks, the second processing step (identifying the site of irradiation and defining the ROI) was accurate in 99% of all cases.

It should be noted that the 100 image stacks included into the analysis also comprise very difficult segmentation scenarios, e.g. cases where the cell moves significantly during image acquisition, or where confounding factors such as air bubbles or other cells (albeit without lesion) are present in the image. A selection of difficult segmentation scenarios where our approach was still mostly successful is shown in Figure 2. Each row shows sample images that were acquired during the experiment and the *avg-t*-projection image of the segmented and registered image stack. Row (a) shows a very good example where the accumulation is clearly visible and the cell hardly moves. Rows (b) and (c) are difficult to segment and to measure due to cell movement and deformation of the nucleus (b) or hardly detectable accumulation (c). Row (d) is another difficult example where the intensity within the nucleus is so high that our algorithm detects a wrong ROI. The ROI detection for all of these image stacks is shown in Figure 3. The top row shows the *avg-t*-projection and the detected ROI is overlaid. The bottom row shows the corresponding intensity profile, the peak that the scoring algorithm chooses is clearly marked. Note that the ROI detection in image (d) failed, the actual accumulation takes place to the left of the detected ROI; this is the only case of all processed image stacks where the ROI detection failed.

The processing time per image stack is in the range of 1–2 minutes per stack on a computer running a 2.83 GHz processor. In the whole processing pipeline, the registration and preprocessing stages are the most time consuming steps.

### B. Manual vs. Automated Analysis

For a more detailed assessment of the results of the automated image processing approach, the automated measurements are compared to the manual evaluation in [6] and [9]. The manual evaluation is done similar to the automated evaluation. First, the image stack is registered, then the ROI is determined manually and the intensity of the ROI in each image of the stack is measured and the quotient  $I_{ROI}/I_{NOI}$  is determined. In contrast to the automated evaluation, the ROI size is not fixed, but adjusted to fit the most visible part of the lesion.

Figure 4 (a) shows the result of our automatic intensity measurements for four different XPC mutants (F756A, F797A, F799A, N754A) and wild-type XPC expressed in CHO cells. The quotient  $I_{ROI}/I_{NOI}$  is plotted versus the time of acquisition. Shown are the mean values of at least 8 image stacks per mutant, the error bar is given by the standard error of these mean values. The computed results are compared to those obtained by manual evaluation [9] as

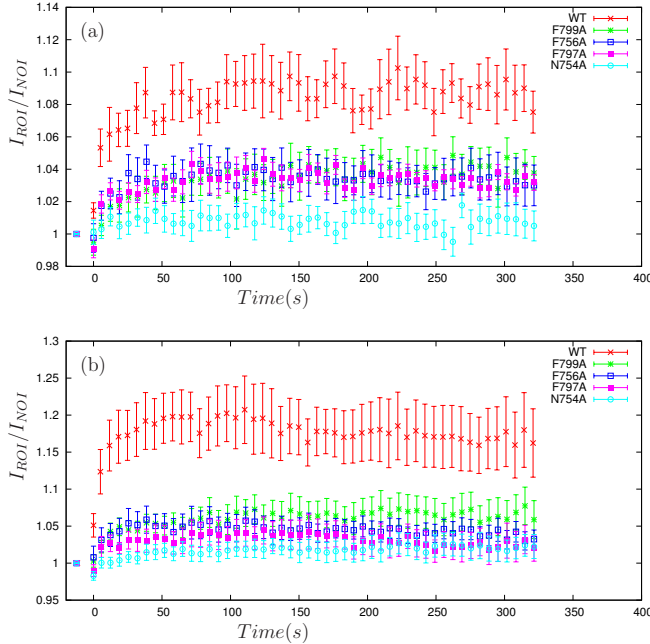


Fig. 4. Results of the automatic measurement (a) and the manual measurement (b). Shown are the mean values and their standard errors of the intensity quotient  $I_{ROI}/I_{NOI}$  of several image stacks for five different XPC mutants in CHO cells.

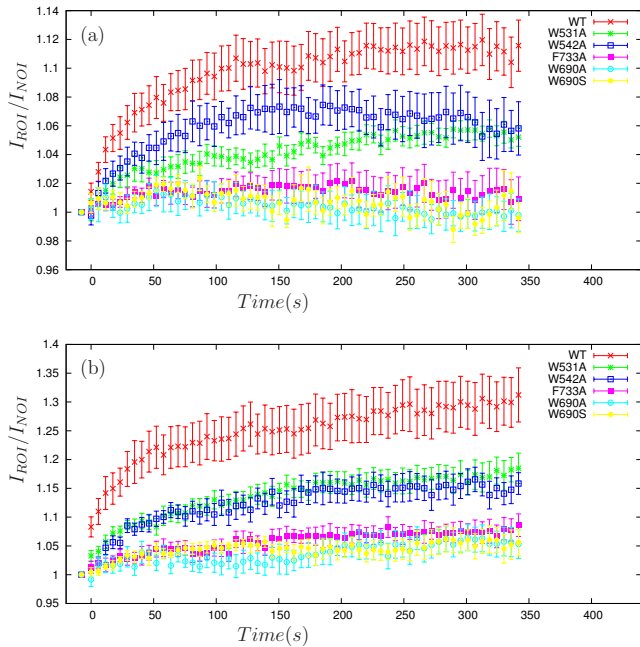


Fig. 5. Results of the automatic measurement (a) and the manual measurement (b). Shown are the mean values and their standard errors of the intensity quotient  $I_{ROI}/I_{NOI}$  of several image stacks for different XPC mutants expressed in XP-C fibroblasts.

shown in Figure 4 (b). Note that the graphs show the same qualitative behaviour, but there is a quantitative difference. The intensity increase determined by the automated approach is much lower. However, at the same time there is a reduction of the standard error, hence preserving e.g. the statistically significant difference between the data from XPC-WT and the various XPC mutants (in this case, the statistical significance is simply provided by non-overlapping standard error bars). What is more, the automatically measured intensity changes of the N754A mutant are lower than intensity changes of the F-mutants. Whether the improved ability of the automated analysis to differentiate between the N and the F mutants has a biological correlate is a question beyond the scope of this work and will be investigated in future studies.

Figure 5 (a) shows the automatically measured intensity changes for five different XPC mutants (W531A, W542A, F733A, W690A, W690S) and wild-type XPC expressed in XP-C cells. The quotient  $I_{ROI}/I_{NOI}$  is plotted versus the time, and again the mean values of several image stacks per XPC mutant are shown. The results of the manual evaluation from [6] are shown in Figure 5 (b); note that the graphs show the same quantitative differences as the graphs in Figure 4. The qualitative features are largely preserved, with the exception that the automatically measured values of W531A and W542A are separated in the time interval starting at 50s and ending at 220s. This separation cannot be seen in the manual evaluation and it is not entirely clear if there are biological reasons for this separation or if it is due to the image quality of the W542A mutants, which is also expressed in the high standard error in the automated analysis result.

Summarizing, the results of the automated measurements preserve the features that were discovered in the manual evaluation, and on top of that have the advantage of reproducibility and unbiasedness, and, last but not least, time saving. Moreover, the measurement seems to be more accurate, the N754A mutant appears clearly separated from the F-mutants in the experiments involving the CHO cells, which is not the case for the manual evaluation.

#### IV. DISCUSSION

The results of our automated image processing approach are very satisfactory. We achieve almost 99 % correctly segmented nuclei and 99 % correctly determined ROIs for our data set of approximately 100 image stacks included in the analysis. Moreover, the comparison with a manual evaluation of the data set shows that the automated measurement not only supports the qualitative statements that can be drawn from the manual evaluation, but also has a lower standard error. In the presented case, the automated evaluation shows that the N754A mutants behave significantly different from the other evaluated mutants. Whether the improved ability of the automated analysis to differentiate between the N and the F mutants has a biological correlate is a question beyond the scope of this work and will be investigated in future studies.

The quantitative differences of the measured intensity values in the manual and in the automated evaluation are likely due to the choice of the ROI size. In the manual evaluation, the ROI

has been chosen smaller for the XPC mutants where the XPC-GFP accumulation is clearly visible, and larger for the XPC mutants where hardly any accumulation is visually detectable. This choice influenced the measured intensity changes, in particular the values for mutants with high accumulation are much higher than in the automated analysis, where the ROI has a constant size throughout the analysis. Although this automated approach performs very well for our experimental data sets, there is room for improvements regarding the registration algorithm — a nonlinear registration algorithm [16] can also compensate deformation of the irradiated area — and computation time.

## V. CONCLUSION

We present an automated system for measuring the performance of XPC in the DNA repair process based on intensity changes in microscopy images. The image processing pipeline comprises several steps that are based on standard image processing algorithms in combination with a customized segmentation algorithm and a specific scoring method to detect the correct ROI.

Laser microirradiation in combination with fluorescence microscopy has become a popular method for studying the dynamics of DNA repair in live cells. Computational tools that facilitate the extraction of quantitative data from such experiments are therefore of great interest to the biology community. Further work will be directed at recognizing more complex irradiation and damage patterns.

## VI. ACKNOWLEDGMENTS

The Interdisciplinary Center for Interactive Data Analysis, Modelling and Visual Exploration (INCIDE) is funded via a grant of the German Excellence Initiative by the German Research Foundation (DFG) and the German Council of Science and Humanities awarded to the University of Konstanz. The Center of Applied Photonics (CAP) is supported by the Ministry of Science, Research and the Arts Baden-Württemberg. We thank D. Träutlein and H. Naegeli for providing image data. We acknowledge the methodical and administrative support by A. Leitenstorfer, M. Horn and O. Deussen.

## REFERENCES

- [1] H. Lodish, A. Berk, P. Matsudaira, C. A. Kaiser, M. Krieger, M. P. Scott, L. Zipursky, J. Darnell, *Molecular Biology of the Cell*, WH Freeman, New York, 2004.
- [2] L. C. Gillet, O. D. Schärer, Molecular mechanisms of mammalian global genome nucleotide excision repair, *Chemical Reviews* 106 (2) (2006) 253–276.
- [3] P. C. Hanawalt, G. Spivak, Transcription-coupled DNA repair: two decades of progress and surprises, *Nature Reviews Molecular Cell Biology* 9 (2008) 958–970.
- [4] O. D. Schärer, Achieving broad substrate specificity in damage recognition by binding accessible nondamaged DNA, *Molecular Cell* 28 (2) (2007) 184–186.
- [5] K. Sugawara, F. Hanaoka, Sensing of DNA damage by XPC/Rad4: one protein for many lesions, *Nature Structural & Molecular Biology* 14 (10) (2007) 887–888.
- [6] U. Camenisch, D. Träutlein, F. C. Clement, J. Fei, A. Leitenstorfer, E. Ferrando-May, H. Naegeli, Two-stage dynamic DNA quality check by xeroderma pigmentosum group C protein, *The EMBO Journal* 28 (2009) 2387–2399.

- [7] Z. Gitai, New fluorescence microscopy methods for microbiology: sharper, faster, and quantitative, *Current Opinion in Microbiology* 12 (2009) 341–346.
- [8] D. Träutlein, F. Adler, K. Moutzouris, A. Jeromin, A. Leitenstorfer, E. Ferrando-May, Highly versatile confocal microscopy system based on a tunable femtosecond Er: fiber source, *Journal of Biophotonics* 1 (1) (2008) 53–61.
- [9] F. Clement, N. Kaczmarek, N. Mathieu, M. Tomas, A. Leitenstorfer, E. Ferrando-May, H. Naegeli, Dissection of the xeroderma pigmentosum group C protein function by site-directed mutagenesis, *Antioxid Redox Signal* (to appear).
- [10] M. R. Berthold, N. Cebon, F. Dill, T. R. Gabriel, T. Kötter, T. Meinl, P. Ohl, C. Sieb, K. Thiel, B. Wiswedel, KNIME: The Konstanz Information Miner, in: *Proc. Data Analysis, Machine Learning and Applications*, 2008, pp. 319–326.
- [11] N. Otsu, A threshold selection method from gray-level histograms, *IEEE Transactions on Systems, Man and Cybernetics* 9 (1) (1979) 62–66.
- [12] P. Bamford, B. Lovell, Unsupervised cell nucleus segmentation with active contours, *Signal Processing* 71 (2) (1998) 203–213.
- [13] M. Kvarnström, K. Logg, A. Diez, K. Bodvard, M. Käll, Image analysis algorithms for cell contour recognition in budding yeast, *Optics Express* 16 (17) (2008) 12943–1257.
- [14] P. Thévenaz, U. Rüttimann, M. Unser, A pyramid approach to subpixel registration based on intensity, *IEEE Transactions on Image Processing* 7 (1) (1998) 27–41.
- [15] R. Lienhart, E. Kuranov, V. Pisarevsky, Empirical analysis of detection cascades of boosted classifiers for rapid object detection, in: *In DAGM 25th Pattern Recognition Symposium, 2003*, pp. 297–304.
- [16] I.-H. Kim, R. Eils, K. Rohr, Non-rigid alignment of multi-channel fluorescence microscopy images of live cells for improved classification of subcellular particle motion, Vol. 7262, *SPIE*, 2009, p. 72620S.